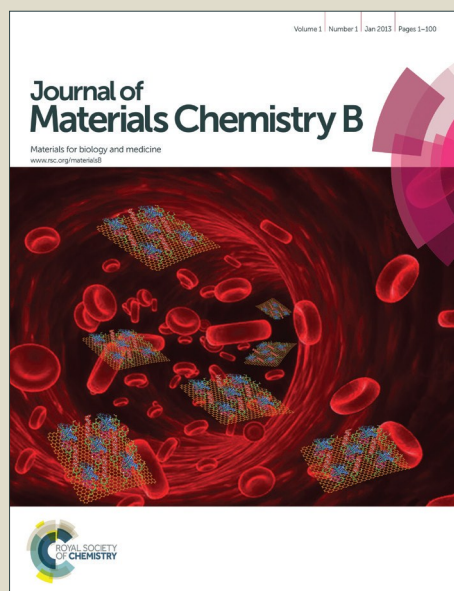


Journal of Materials Chemistry B

Accepted Manuscript



This is an *Accepted Manuscript*, which has been through the Royal Society of Chemistry peer review process and has been accepted for publication.

Accepted Manuscripts are published online shortly after acceptance, before technical editing, formatting and proof reading. Using this free service, authors can make their results available to the community, in citable form, before we publish the edited article. We will replace this *Accepted Manuscript* with the edited and formatted *Advance Article* as soon as it is available.

You can find more information about *Accepted Manuscripts* in the [Information for Authors](#).

Please note that technical editing may introduce minor changes to the text and/or graphics, which may alter content. The journal's standard [Terms & Conditions](#) and the [Ethical guidelines](#) still apply. In no event shall the Royal Society of Chemistry be held responsible for any errors or omissions in this *Accepted Manuscript* or any consequences arising from the use of any information it contains.

Fluorescent ZnO for imaging and induction of DNA fragmentation and ROS-mediated apoptosis in Cancer cells

Jagriti Gupta, Parag Bhargava and D. Bahadur*

Department of Metallurgical Engineering and Materials Science,
Indian Institute of Technology Bombay, Mumbai – 400076, India

*Corresponding address: Tel. + 91-22-2576 7632, Fax: + 91-22 2572 3480, Email: dhiren**b**@iitb.ac.in

Abstract

Fluorescein isothiocyanate (FITC)-encapsulated ZnO nanocomposite has been synthesized using the soft chemical approach. X-ray diffraction reveals the formation of highly crystalline single-phase hexagonal wurtzite nanostructure. TEM and SEM micrographs indicate the formation of spherical porous nanoassembly of ZnO of size ~ 100-400 nm. On the other hand FITC-ZnO nanocomposite is spherical and porous but with a uniform size of ~ 150 nm. The size of single particles is ~ 20 nm for the ZnO nanoassembly and ~ 15 nm for FITC-ZnO nanocomposite. The UV-visible, fluorescence, FTIR and XPS spectra confirm the formation of FITC-ZnO nanocomposite. The FITC-ZnO nanocomposite demonstrates excellent selectivity in preferential killing of cervical (HeLa) and breast (MCF-7) cancer cells with minimal toxicity to normal fibroblast cells (L929). Apoptotic cells are observed and analyzed by confocal microscopy and flow cytometry. Our results show that cytotoxicity of FITC-ZnO nanocomposite towards cancer cells is due to the generation of reactive oxygen species (ROS) and preferential dissolution of Zn^{2+} ions in acidic cancer microenvironment. Furthermore, generated ROS and dissolved Zn^{+2} ions induce cellular apoptosis, the DNA fragmentation, and depolarization of mitochondrial membrane and cell cycle arrest in S phase. The FITC encapsulated multifunctional ZnO nanocomposite can be used as smart nanostructures for cell imaging, and cancer therapy.

Keyword: fluorescent ZnO; nanocomposite; ROS; bioimaging; cancer therapy.

1. Introduction

ZnO is one of the most diverse among the family of the semiconductor oxides which can be used not only in the field of electronics, but also for biomedical applications such as biosensors, bioimaging, cancer therapeutics and bacterial treatment [1-6]. ZnO is used as efficient catalyst for the removal of contaminants and for the treatment of bacteria from the waste water [7-9]. ZnO nanoparticles provide new platforms for biomedical applications and therapeutic intervention. It is generally biocompatible and biodegradable at low pH which is an important criterion for biomedical applications [10]. Mesoporous ZnO has been used for *in vitro* drug delivery for cancer [11]. Also, many of the reports talk about the biocompatible nature of ZnO nanoparticles. Recently, however, much attention has been paid to use ZnO as a toxic material and as an alternative source towards cancer therapy and cell labelling as discussed below [4]. The attractive nanoscale properties of metal oxides make them a good candidate for *in vitro* and *in vivo* studies [12, 13]. However, cellular toxicity of these nanoparticles is often higher due to their increased surface reactivity which allows them to readily interact with biomolecules on cell surfaces as well as within the cell [14]. This characteristic makes the metal oxide nanomaterials attractive for use in biomedical applications. It has also been proposed that the higher surface area of metal oxide nanoparticles significantly enhances their ability to produce reactive oxygen species (ROS) [15, 16]. Toxicity of ZnO is reported due to the generation of intracellular reactive oxygen species (ROS), and dissolved Zn ions [17-23]. ROS are generated through various mechanisms such as illumination of nanomaterials by UV light, disturbance of intra-cellular metabolic activities, and the anti-oxidant system, result the generation of oxidative stress in the cells. ROS can damage DNA, cell membrane and proteins which may lead to cell death [24, 25]. Li *et al.* and Xia *et al.* reported that the toxic behavior of ZnO is related to the generation of reactive oxygen species and release of Zn²⁺ ions in the lysosome [21, 26]. Dissolved Zn ions affect the mitochondrial function which leads to the apoptosis of the cancer cells. Again, the generation of hydrated zinc ions causes mitochondrial damage and disruption

of cellular zinc homeostasis leading to cell death [27]. Premanathan *et al.* and Ostrovsky *et al.* reported the toxicity of ZnO nanoparticles preferentially towards cancer cell (HL60) and glioma cells as compared to the normal cells [28, 29]. They explained the toxicity of ZnO nanoparticles due to the generation of ROS and induction of apoptosis. Akhtar *et al.* also demonstrated that ZnO nanoparticles selectively induce apoptosis in cancer cell through the generation of ROS via p53 pathway [30]. Guo *et al.* described that the generation of ROS in rat retinal ganglion cells was primarily responsible for cell death [31]. Also, in a more recent work, Punnoose *et al.* attributed this toxicity to the surface chemistry of the ZnO nanoparticles [32]. Most of the recent studies focused towards the toxicity of nanorods and nanoparticles of ZnO [23, 28]. It is expected that the nanoassembly of ZnO will be more efficient for the treatment of cancer cells due to their high surface area and surface reactivity compared to single nanoparticle system.

Development of porous nanomaterials that can accommodate both dyes and drug making them multifunctional, are of great interest for future nano-bio-technology and biomedical applications. Burns *et al.* and Guo *et al.* reported that the fluorescent dye encapsulated in the pores of silica and the core shell structure track the delivery of drugs at the site of interest [33, 34]. Similarly, YVO₄ encapsulated mesoporous SiO₂ structure has been reported as a useful drug delivery system with imaging capabilities [35]. Many of the fluorescent dyes are widely used for cell imaging as well as model drug. But, these are very sensitive to the environment and often interact with solvent molecules present in the environment, which retards their performance. To resolve this problem, we report for the first time the synthesis of fluorescent dye encapsulated mesoporous ZnO nanoassembly to protect it from photo bleaching while maintaining their fluorescence properties under acidic environment. Herein, we use a facile single-step process for preparation of fluorescein isothiocyanate (FITC) encapsulated mesoporous ZnO nanocomposite. In this work, we investigate the toxicity mechanism of FITC-ZnO nanocomposite towards cancer cells. For this, we employed three different cells, normal fibroblast cell (L929), cervical (HeLa) and

breast (MCF-7) cancer cells. Two representative cancer cells, cervical (HeLa) and breast (MCF-7) cancer cells were chosen for preferential toxicity studies of FITC-ZnO nanocomposite. Specifically, we explore the toxic behavior of FITC-ZnO nanocomposite and systemically study the mechanism of toxicity towards the cancer cells.

2. Experimental

2.1 Synthesis

Porous nanostructures of ZnO were prepared by refluxing of zinc acetate dehydrate in diethylene glycol (DEG) medium. 0.01 moles of acetate precursors were added to 100 ml DEG and heated under reflux conditions. ZnO particles were precipitated out shortly after reaching the temperature of 160-170 °C. At this temperature, the reaction mixture was stirred for ½ h, after which the reaction vessel was cooled to room temperature. In order to prepare FITC encapsulated ZnO, 5 mg of FITC was added to the reaction mixture under refluxing. The samples were washed with acetone, methanol and water 2-3 times and dried at 80 °C for 1 h prior to further characterization. The pure and FITC encapsulated ZnO samples are termed as ZnO and FITC-ZnO nanocomposite, respectively.

2.2 Characterization

X-ray diffraction (XRD) patterns were recorded on a PANalytical's X'Pert PRO diffractometer with Cu K α radiation. The crystallite sizes were estimated using Scherrer's calculator of X'Pert High Score Plus software. The electron microscopy images were taken by Philips CM 200 transmission electron microscopy (TEM) and scanning electron microscopy (SEM). The energy dispersive spectroscopy (EDS) analysis was carried out by using the EDS facility of S-3400N SEM. UV-visible spectra were recorded with a UV-visible spectrophotometer (Cecil, Model No. CE3021). The fluorescence spectra of samples were recorded using Hitachi F 2500 fluorescence spectrophotometer. The elemental analysis was carried out by FLASH EA 1112 series CHNS (O) analyzer (Thermo Finnigan, Italy). XPS analysis was performed on a Multilab 2000 (Thermo VG Scientific) using Al K α ($h\nu = 1486.6$ eV) as the exciting source for identification of the elements and chemical status with the

electronic database. The binding energies obtained in the XPS analysis of samples were standardized for specimen charging using C (1s) as the reference at 285 eV.

2.3 Cytotoxicity Study

Sulforhodamine B (SRB) assay was performed to evaluate cytotoxicity of the FITC-ZnO nanocomposite with normal fibroblasts cells (L929), human cervical cancer cells (HeLa) and breast cancer cells (MCF-7). The cells were seeded into 96 well plates at density of 1×10^4 cells per well for different time periods. Different concentrations of FITC-ZnO nanocomposite were added to the cells and incubated for different time periods at 37 °C and 5 % CO₂. Thereafter, the cells were washed thrice with phosphate buffer saline (PBS) and processed for SRB assay to determine the cell viability. Further, cells were fixed with a solution of 10% trichloroacetic acid and stained with 0.057% SRB and washed with 1% acetic acid. Cell-bound dye was extracted with 10 mM tris buffer solution (pH 10.5) and then absorbance was measured at 560 nm using a plate reader. The cell viability was calculated using the following formula:

$$\% \text{ Viability} = (\text{Absorbance of sample} / \text{Absorbance of control}) \times 100$$

2.4 Cellular uptake

Cellular uptake experiment was performed in the 6 well plate, with nearly 1×10^5 cells per well. After 24 h, the cells were washed with PBS and treated with different concentration of FITC-ZnO nanocomposite and incubated for 6 h. After incubation, cells were washed with PBS three times to remove unbound FITC-ZnO nanocomposite. Cells were then trypsinized using 1 ml/well trypsin. Trypsinized cells were centrifuged at 3000 rpm for 5 min and the cell plate was dissolved in dilute HCl. Cellular uptake studies were undertaken on different cell lines using 100 µg/ml of FITC-ZnO nanocomposite.

2.5 Measurement of Reactive Oxygen Species (ROS)

For the determination of ROS, 5, 5-dimethyl-1-pyrroline-N-oxide (DMPO) and 2, 2, 6, 6-tetramethylpiperidin (TEMP) is used as spin trapper by electron spin resonance (ESR). We measured hydroxyl radicals from FITC-ZnO nanocomposite (10 mg/mL) with DMPO (1.5 M)

and DMPO with dimethylsulfoxide (DMSO, 10%; as a hydroxyl radical scavenger). For singlet oxygen measurement, we mixed FITC-ZnO nanocomposite (10 mg/mL) with TEMP (4.7 mM) and NaN₃-treated FITC-ZnO nanocomposite with TEMP [36]. NaN₃ serves as singlet oxygen scavenger. Intracellular ROS is also measured using 2, 7, dichlorodihydrofluorescein diacetate (H₂-DCFDA) with/without N-acetylcysteine (NAC as ROS scavenger, 10 mM) and the images were captured by confocal laser scanning microscopy (CSLM). Briefly, 5 μM H₂-DCFDA dye solution was prepared in DMEM media. After 24 h incubation with 100 μg/ml of FITC-ZnO nanocomposite, the cells were washed with phosphate buffered saline (PBS) and H₂-DCFDA dye solution was added for 30 min. Again cells was washed with the PBS and fixed with 4 % paraformaldehyde. For another experiment for detection of ROS, MCF-7, HeLa and L929 cells were seeded in 96-well plates at a concentration of 1×10^4 cells/ml for 48 h for the attachment of the cells followed by treatment with FITC-ZnO nanocomposite. Same experiment is also performed in the presence of N-acetyl cysteine (NAC). N-acetyl cysteine (NAC) was added to the cells at concentration of 10 mM for 2 h. After NAC pretreatment, cells were washed with PBS and treated with the different concentration of FITC-ZnO nanocomposite. ROS is determined by adding H₂DCFDA to pretreated cell cultures and recording the dichlorofluorescein (DCF) fluorescence at 535 nm. Detection of ROS measurement was repeated 3 times independently. After the background subtraction, fluorescence intensity of DCF is recorded by the plate reader and expressed as ratio of fluorescence of DCF of treated cell to the fluorescence of DCF of untreated cell.

2.6. Evaluation of death mechanisms in HeLa and MCF-7 cells by Annexin V-FITC and PI assay

An Annexin V-FITC and PI assay is used for the detection of apoptotic cells. The assay procedure is according to the instruction of Annexin V-FITC apoptosis detection kit (Invitrogen). 1×10^6 cells per experiment have been taken. After 24 h, cells were treated with 100 μg/ml of FITC-ZnO nanocomposite for next 24 h. Then, cells are washed with cold PBS,

centrifuged and the supernatants were removed. Cell plates were again resuspended in 100 μl of binding buffer and added 5 μl of Annexin V-FITC and 1 μl of propidium iodide (PI) at room temperature in the dark. After incubation for 30 min at room temperature in the dark, stained cells were diluted by the same binding buffer and directly analyzed by the fluorescence-activated cell sorting method (FACS, BD FACS Aria, USA).

2.7. Cell cycle analysis

The effect of FITC-ZnO nanocomposite on the cell cycle of HeLa cells was analyzed by staining the DNA with propidium iodide and using flow cytometry. In brief, 1×10^6 cells were seeded in the 6-well plate. After 24 h, cells were treated with the 50 and 100 $\mu\text{g/ml}$ of FITC-ZnO nanocomposite for 24 and 48 h. After treatment, Cells were trypsinized, washed with ice-cold PBS and fixed in ice-cold 70% ethanol for 1 h at 4 $^{\circ}\text{C}$. Before flow cytometry analysis, cells were washed in PBS and stained with RNase (20 $\mu\text{g/ml}$) for 1 h at 37 $^{\circ}\text{C}$ and PI was added (20 $\mu\text{g/ml}$) for 30 min and analyzed by flow cytometric measurement. Collected Data was analyzed using Modfit software.

2.8. Cell morphological assessment of apoptosis

For the detection of morphological evidence of apoptosis, the cell nuclei were visualized following DNA staining using fluorescent nuclear dye, ethidium bromide (EtBr). For this analysis, cells were seeded at a concentration of 1×10^5 cells per well on the cover slip in 24 well plates and treated with 100 $\mu\text{g/ml}$ of FITC-ZnO nanocomposite for different time periods (3, 24 and 48 h). After the desired incubation time, the cells were washed thoroughly with PBS, fixed with 70% ethanol and incubated with EtBr (10 mM) for 5 min. The cells were again washed with PBS, mounted on a glass slide and then examined with an IX81 FV500 laser scanning confocal microscope.

2.9. Mitochondrial membrane potential assessment and Lactate dehydrogenase (LDH) release

Mitochondrial membrane potential (MMP) was assessed by using JC-10 dye mitochondrial membrane potential assay kit having (Sigma-Aldrich). In this typical

experiment, 1×10^4 cells were seeded in 96 well plates and treated with 50 and 100 mg/ml of ZnO nanoassembly for 24 h. After treatment, the cells were washed with PBS and the JC-10 dye was added according to the instruction given in JC-10 dye mitochondrial membrane potential assay kit. The ratio of red/green fluorescence intensity was used to determine the MMP. For the LDH activity in extracellular medium due to membrane damage was assessed by using LDH kit (Sigma-Aldrich). For this experiment, 1×10^6 cells were seeded in 6 well plates and treated with 50 and 100 mg/ml of FITC-ZnO nanocomposite for 24 h and the measurement of LDH release were done according to the instruction given in the LDH kit.

3. Statistics

The data are expressed as the mean \pm SD (standard deviation) from three independent experiments ($n=3$). One tailed unpaired Student's t-test (Microsoft excel) was used for significance analysis, and $p < 0.05$ (*) and 0.001 (**) are considered significant as compared to control.

4. Results and discussion

Fig. 1(a) shows the XRD patterns of ZnO and FITC-ZnO nanocomposite. The XRD analysis revealed that ZnO and FITC-ZnO nanocomposite exhibit single phase hexagonal wurtzite structure. The crystallite size was estimated from X-ray line broadening using Scherrer's formula and was found to be ~ 20 and ~ 15 nm for ZnO and FITC-ZnO nanocomposite, respectively. Fig. 1(b) shows the three most intense diffraction peaks of ZnO and FITC-ZnO nanocomposite which show shifting and broadening of diffraction peaks of FITC-ZnO nanocomposite to higher angle with respect to pure ZnO. The broadening of XRD lines suggest that the crystallite size of ZnO is reduced possibly due to the interaction of FITC with ZnO. This interaction may also be responsible for a slight shift of the diffraction line to higher angle.

Fig. 2 shows the SEM micrographs of (a) ZnO, and (b) FITC-ZnO nanocomposite. Their corresponding TEM micrographs are shown in Fig. 2 (c and d). From SEM micrographs, spherical nanoassembly of ZnO having diameter in the range of ~ 100 - 400 nm

are observed whereas the FITC-ZnO nanocomposite has a diameter ~ 150 nm. It is also observed that the pristine ZnO nanoassembly is larger than those of FITC-ZnO nanocomposite. From the TEM micrographs, it is seen that these spheres are well-defined, discrete and porous. Each sphere is made up of three-dimensionally (3D) spatially connected numerous irregular shaped nanocrystals of the size of 10-20 nm, which is in a good agreement with the crystallite size obtained from XRD line broadening. Surface area and pore size distribution were recorded for ZnO and FITC-ZnO nanocomposite to find out the textural nature of ZnO and their composite with FITC. The Brunauer-Emmett-Teller (BET) surface area and pore volume of ZnO nanoassembly and FITC-ZnO nanocomposite were found to be 20.6 and 43.51 m^2/gm , and 0.22 and 0.19 cm^3/gm , respectively (see ESI Fig. S1). Increase in the surface area and decrease in the pore diameter suggest the formation of smaller average crystallites due to the incorporation of FITC into ZnO structure which is also in agreement with the XRD and TEM results. The colloidal stability of FITC-ZnO nanocomposite is investigated by UV-visible spectra with different cell culture media. FITC-ZnO nanocomposite shows good colloidal stability (see ESI Fig. S2).

Fig. 3(a) shows the UV-visible spectra of FITC, ZnO and FITC-ZnO nanocomposite. The UV absorption band observed at 374 nm in pure ZnO is shifted to lower wavelength at 367 nm in FITC-ZnO nanocomposite. The absorption peak due to FITC (λ_{abs} at 488 nm) observed in FITC-ZnO nanocomposite is slightly shifted towards the higher wavelength at 493 nm. This small red shift in the absorption peak in FITC-ZnO nanocomposite suggests a chemical interaction between FITC and ZnO nanoassembly. This is also evident from the FTIR spectra, TGA analysis and XPS spectra. From the FTIR spectra, a band at 2112 cm^{-1} (characteristic peak of N=C=S peak) in FITC slightly shifted to 2116 cm^{-1} , confirms the presence of FITC in ZnO (See ESI Fig. S 3a). The weight loss of about 4.7 % in ZnO above 150 $^{\circ}\text{C}$ is attributed due to removal of water and acetate groups adsorbed on the surface of ZnO. The weight loss of about 5.7 % above 350 $^{\circ}\text{C}$ in case of FITC-ZnO nanocomposite is possibly due to removal of organic molecules of FITC (see ESI Fig. S 3b). From the XPS

spectra (see ESI Fig. S 3c), it is observed that the Zn $2p_{3/2}$ peak is shifted from 1021 to 1022.2 eV in FITC-ZnO nanocomposite, which can be attributed to the reduction of Zn valence due to electron transfer from the FITC *via* donation of lone pair of electron to the Zn⁺⁺ [37]. This further suggests that the FITC is bound to the ZnO nanoassembly by chemical bonding. Fig. 3(b) shows the fluorescence spectra of FITC, ZnO and FITC-ZnO nanocomposite. Appearance of a strong emission peak of pure FITC at 520 nm in FITC-ZnO nanocomposite indicates the successful embedment of FITC in ZnO nanoassembly. Pure FITC shows a broad band in the range of 450-600 nm with maxima at 520 nm. This is also found in FITC-ZnO nanocomposite. However, the defect related emission in the green region (~ at 520 nm) is not observed in the pure ZnO nanoassembly. This observation suggests that encapsulation of FITC in the ZnO nanoassembly helps in the size reduction of ZnO nanoassembly as well as in the production of some defects due to the reduction of in ZnO nanoassembly. Encapsulation of FITC in the ZnO nanoassembly is responsible for the green emission in FITC-ZnO nanocomposite. Enderlein *et al.* [38] reported that when a fluorophore comes in contact with a metal layer, photo stability as well as its fluorescence properties is enhanced due to the decrease of its fluorescence life time. To overcome this problem of varying fluorescence in various environments, the fluorophore may either be encapsulated inside a porous carrier or within the core-shell structures which protect them from photo bleaching while maintaining their fluorescence properties. The present mesoporous ZnO nanoassembly has proven themselves to be a potential answer to this challenge. ZnO nanoassembly not only protects the interaction of FITC molecule from its microenvironment but also protects its fluorescence. Under the influence of low pH, the fluorescence phenomenon in FITC is known to decrease. Fig. 4 shows the pH dependent fluorescent intensity change of pure FITC and FITC-ZnO nanocomposite. Our pH-dependent results have shown that only a meager decrease of ~15% in the fluorescence is observed in ZnO conjugated FITC as against ~80% decrease in free FITC molecules. Thus, in addition to its therapeutic and imaging capabilities, ZnO

nanoassemblies has successfully given shelter to the FITC molecules within its mesoporous structure and increase its fluorescence longevity *in vitro*.

Fig. 5(a) bright field and (b) fluorescence micrograph of HeLa cells show the uptake behavior FITC-ZnO nanocomposite after 3 h incubation. FITC-ZnO nanocomposite is passively loaded into HeLa cells by incubating them with 100 $\mu\text{g/ml}$ of the nanocomposite. The confocal images clearly demonstrate that FITC-ZnO nanocomposite has an excellent ability to image cells using common imaging techniques if they can be attached to the cells of interest. This image indicates that many of these FITC-ZnO nanocomposite associated HeLa cells are still viable even though the FITC-ZnO nanocomposite can be toxic to HeLa cells. This is likely due to the short incubation time (3h) of FITC-ZnO nanocomposite with the cells for imaging. The uptake of FITC-ZnO nanocomposite in HeLa, MCF-7 and L929 cells was confirmed by ICP-AES analysis. Fig. 5 shows the cellular uptake study of FITC-ZnO nanocomposite incubated for 3 h in (c) HeLa and MCF-7 cells and (d) L929 cells. The cellular uptake of particles was also quantified by measuring the zinc content per cell using ICP-AES which shows that the internalization of the particles is dependent on the concentration. Some extracellular larger bright spots are seen. We believe that these could possibly be debris of the cells. Some aggregation of particles is not ruled out. ICP-AES result shows that 0.5 mg/ml of FITC-ZnO nanocomposite have 936.5, 915.9 and 5.6 pg/cells of Zn ions inside HeLa, MCF-7 and L929 cells, respectively. From the ICP-AES results, the cancer cells show higher uptake as compared to normal cells. The internalization result is in a good agreement with the findings by Laser scanning confocal microscopy (LSCM) images.

ROS has the ability to produce oxidative stress that damages the cellular component such as cell membranes, DNA, and cellular proteins, and may lead to cell death [18, 31]. Hydroxyl radical ($\text{OH}\cdot$) is one of the most reactive oxygen radicals that reacts very quickly with molecules found in viable cells. The presence of intracellular ROS was determined by using H_2DCFDA staining, microplate assay and ESR spectroscopy. $\text{H}_2\text{-DCFDA}$ is well known cell-permeate indicator for ROS. It is non fluorescent dye until the acetate groups are

removed by intracellular esterase and oxidation occurs within the cell, resulting in a reduced intermediate that can subsequently be oxidized in the presence of ROS and thus fluoresces. The production of intracellular ROS in HeLa, MCF-7 and L929 cells was measured by microplate assay after incubation with FITC-ZnO nanocomposite for 48 h. Fig. 6(a and b) shows significant increase in ROS production in HeLa and MCF-7 cells treated with FITC-ZnO nanocomposite. In the presence of N-acetyl cysteine, production of ROS is decreased with increase of FITC-ZnO nanocomposite concentration. Fig. 6(c) shows the ROS production in L929. The production of ROS in L929 cells is much less as compared to cancerous cells. Fig. 7(a-h) shows the intracellular ROS generation by CLSM image of HeLa cells. From the CLSM images, the green fluorescence depicts the presence of intracellular ROS in the cells due to the formation of DCF (oxidized form of H₂-DCFDA). Therefore, this confirms the release of intercellular ROS in HeLa cells. If the free radical scavenger, NAC (10 mM) was added to the culture medium, the green fluorescence is quite less when treated with FITC-ZnO nanocomposite. Thus, it is possible that the FITC-ZnO nanocomposite generated the ROS in a cell through free radical formation. Production of ROS in FITC-ZnO nanocomposite is also confirmed by ESR spectroscopy (See ESI Fig. S5). Fig. S 4(a) shows the generation of hydroxyl radical in FITC-ZnO nanocomposite in water suspension with DMPO and DMPO with 10 % DMSO. ROS has a very short half-life which makes its detection difficult. For detection of ROS, spin trapping agents were used which react with the ROS and form long lived free radicals called spin adducts. They can be easily detected by the ESR spectra. DMPO reacts with hydroxyl radicals and form a paramagnetic free radical DMPO-OH which is relatively stable and can easily be detected by ESR technique. For the detection of singlet oxygen, TEMP was used as spin trapper. TEMP reacts with the singlet oxygen and produce TEMPO, which shows triplet EPR spectra. Fig. S 4(b) shows the ESR spectrum of the FITC-ZnO nanocomposite suspension recorded with TEMP and NaN₃ treated FITC-ZnO nanocomposite, using TEMP as the spin trap. We do not observe any change. This means that no singlet oxygen is generated. Our results show that the FITC-ZnO

nanocomposite generates the hydroxyl radicals. The generation of hydroxyl radical instead of singlet oxygen is also confirmed by ESR spectra

Here, we demonstrate the ability of FITC-ZnO nanocomposite for potential use in biomedical applications especially in cancer cells treatment. Effects of FITC-ZnO nanocomposite on the mortality of HeLa, MCF-7 and L929 cells were assessed using SRB assay. Fig. 8(a) shows the time and dose dependent study of HeLa cells. From the time dependent study, it is observed that the HeLa cell line is 60% viable after a treatment for 6 h and ~ 10% viable after a treatment for 48 h, if treated with 0.5 mg/ml of FITC-ZnO nanocomposite. Fig. 8(b) shows the time and dose dependent study of MCF-7 cells. Similar toxicity is also observed for the MCF-7 cell lines. Fig. 8(c) shows the cell viability of L929 cell line incubated with ZnO nanoassembly and FITC-ZnO nanocomposite at different concentrations (0.0078 to 0.5 mg/ml) after 24 h incubation. Interestingly, we observed that ZnO nanoassembly and FITC-ZnO nanocomposite show no significant toxicity to normal fibroblast (L929) cells after the treatment for 24 h, whereas FITC-ZnO nanocomposite shows cell specific toxicity to the cancer cell lines viz. both HeLa and MCF-7 cells. The developed fluorescent nanocomposite is found to be more toxic for the HeLa and MCF-7 cells. For understanding the potential of the FITC-ZnO nanocomposite for therapeutic applications, 50% inhibitory concentration (IC_{50}) is evaluated by SRB assay. IC_{50} is defined as the concentration of material that results in a 50% inhibition of cellular processes and represents the best efficiency dosage. From Fig. 8(a and b) the relevant IC_{50} values of FITC-ZnO nanocomposite is 16.2 $\mu\text{g/ml}$ for HeLa cells and 23.8 $\mu\text{g/ml}$ for MCF-7 cells. Our cytotoxicity results demonstrate that this FITC-ZnO nanocomposite can significantly inhibit cancer cell proliferation *in vitro* at higher concentrations and have little effect at lower concentrations. Fig. S6 (a) shows the optical micrograph of control HeLa cells without any treatment and Fig. S6 (b and c) shows optical micrographs of HeLa cells treated with 0.007 and 0.5 mg/ml of FITC-ZnO nanocomposites. These micrographs show that 0.5 mg/ml of FITC-ZnO

nanocomposite induces massive cell death of cancer cells with change in cell morphology as compared to 0.007 mg/ml of FITC-ZnO nanocomposite.

In order to quantitatively analyze apoptotic cells under treatment with FITC-ZnO nanocomposite, FACS analysis has been employed using FITC-Annexin and PI staining. Fig. 9 shows the FACS results of (a) control cells without any treatment and (b) cells treated with 100 $\mu\text{g/ml}$ of FITC-ZnO nanocomposite. From the FACS analysis, it has been observed that no apoptosis occurs after 24 h exposure in the control of HeLa cells. On the other hand, for the cells treated, $\sim 93\%$ apoptotic cells are observed after 24 h exposure. MFC-7 cells also show $\sim 83\%$ apoptotic cells on treatment with similar concentration of nanocomposites (see ESI Fig. S 6a and b). Confocal images further confirmed the apoptotic cells staining nucleus by ethidium bromide. Interestingly, we found a good relationship between the antitumor activity of the FITC-ZnO nanocomposites and the stimulation of apoptosis through the generation of ROS. The FITC-ZnO nanocomposites gave green fluorescence due to the presence of FITC. Fig. 10(a) shows that the HeLa cells from the control group exhibited evenly stained nuclei and intact nuclear membranes showing 99% cell viability. In contrast to this, Fig. 10(b to d) shows that FITC-ZnO nanocomposites exhibit loss of cell membrane integrity, complete DNA fragmentation and a reduction in the size of the nucleus as time of treatment increases from 3 to 48 h. These are the most prominent morphological changes used for the identification of apoptosis in cancer cells. Similarly, DNA fragmentation and disruption in nucleus is also observed in MCF-7 cells (See ESI Fig. S 7 for MCF-7 cells). Furthermore, from the optical micrograph, it is observed that all the cells have undergone morphological changes to nearly spherical shape and lost adhesion to the cell culture plate. The observed level of cellular shrinkage or rounding shows further indication of morphological features of apoptotic cell (See ESI Fig. S 5). In addition, mitochondrial depolarization of cancer cells treated with ZnO nanoassembly was also studied using a JC-10 dye. Fig 11(a) shows the mitochondrial membrane potential of HeLa cells using the dye. The marked decrease in mitochondrial membrane potential is evident by a shift in JC-10

fluorescence from red to green. It is observed that 36.4% cells undergo a change to a depolarized state on treatment with 100 $\mu\text{g/ml}$ of ZnO nanoassembly as compared to the control cells. Control cells with functional mitochondria showed red JC-10 aggregates while the apoptotic cells gave evidence of impaired mitochondria containing green JC-10 monomers. Thus, the cells treated with ZnO nanoassembly exhibited increase in the bright green fluorescence with a marked decrease in red fluorescence indicating a loss of MMP. Destabilization of mitochondrial membrane potential in cancer cells leads to the generation of reactive oxygen species and release of Zn^{2+} ions. Under normal condition, mitochondria of cancer cells are hyperpolarized i.e. highly polarized membrane potential leading to an apoptosis-resistant state in cancer. Thus ZnO nanoassembly alters this hyperpolarized state of cancer cells and forces them to undergo apoptosis. Along with the depolarization of mitochondrial membrane potential, injury to the cell membrane is also indicated by an increased LDH release due to the generation of ROS (Fig. 11b). Additionally, the effect of generation of ROS on the cell cycle progression of HeLa cells by the FITC-ZnO nanocomposite can be seen by the DNA damage. Cells usually grow as gap1 (G1), S phase and the G2 phase. Thus the toxic effect of FITC-ZnO nanocomposites was further evident for the cell cycle analysis to detect cell cycle arrest, and evidence of DNA damage. The influence of FITC-ZnO nanocomposites on the cell cycle was analyzed by subjecting cells with nanoparticles to flow cytometry. Fig. 12(a and d) shows the cell cycle of HeLa cells without any treatment for 24 and 48 h. Fig. 12(b,c,e and f) shows the cell cycle of HeLa cell on treatment with two different concentration of FITC-ZnO nanocomposite (50 and 100 $\mu\text{g/mL}$) for 24 and 48 h, respectively. The HeLa cells show a concentration and time dependent S phase arrest which was observed as an increase in cell population in S phase as compared to control. The FITC-ZnO nanocomposites (50 and 100 $\mu\text{g/mL}$) marked the onset of S phase arrest. For the controls, the major cell populations are observed in G1 phase, whereas for the FITC-ZnO nanocomposite treated cells, a decrease in G1 population accompanied by an increase in S phase population is detected. The proportion of cells in G2/M phase is less

affected as compared to the S phase population. Some nanoparticles can cause cell cycle arrest in the different phase in response to DNA damage. Single-walled carbon nanotubes and C (60) fullerenes show the G1 arrest in mouse lung epithelial cells [39]. On the other hand, S and G2/M phase arrest was reported on Jurkat T cells and G2/M phase arrest and DNA damage in human glioblastoma cells and fibroblasts on treatment with Ag nanoparticles [40, 41]. Sasidharan *et al.* reported the S phase arrest of KB cancer cell on treatment with ZnO nanocrystals [17]. Song *et al.* also reported that copper oxide nanoparticles has an ability to induce the cell apoptosis and cell cycle arrest in S phase on the primary human umbilical vein endothelial cells (HUVECs) [42].

The toxic effect of ZnO is not completely understood. Some studies on the toxicity of ZnO nanoparticle are ascribed due to the generation of ROS or the dissolution of metal ions as the main cause [23, 26, 31]. This study suggests that not only generation of ROS is responsible for the toxicity of ZnO but dissolution of Zn^{2+} in the acidic cancer microenvironment is also played a major role in the cytotoxicity of ZnO. Fig. S8 shows the dissolution of FITC-ZnO nanocomposite in cell culture medium in different pH 4.5, 5.6 and 7.4 incubated for 24 h analyzed by ICP-AES analysis. The dissolution assay of FITC-ZnO nanocomposite in different pH conditions has been studied and it revealed that ~ 89.6 and 76.2 % of FITC-ZnO nanocomposite dissolved at pH-4.5 and 5.6 respectively if incubated for 24h at 37 °C whereas only 15.3 % of FITC-ZnO nanocomposite dissolved at normal pH 7.4. This suggests that the acidic microenvironment of cancer cells helps in the preferential dissolution of FITC-ZnO nanocomposite which leads to the possibility of Zn^{2+} poisoning. Metal ions dissolution, in the present case, is more prominent due to the high surface reactivity and surface area of the nanoassembly. Therefore, we have seen that the FITC-ZnO nanocomposite plays a very pivotal role in determining its toxicity which is responsible for the elevated generation of ROS by this material. The surface area and surface reactivity of this nanocomposite is very high as against single nanoparticle system which provides larger interfacial interaction for ROS generation. As mentioned earlier, the defect modalities in its crystal may also be

responsible for the initiation of a variety of toxic reactive oxygen species. Interestingly, the present results revealed that the generation of ROS and dissolution of Zn^{2+} in cancer cells due to FITC-ZnO nanocomposite was significantly higher compared to that in normal cells. ZnO can be dissolved in the acidic environments of the intracellular lysosomal compartments of the cancerous cells. Dissolution of ZnO in cellular acidic microenvironment suggests that higher concentration of Zn^{2+} are able to reduce the mitochondrial respiration due to the generation of reactive oxygen species (ROS) leading to cell death of the cancer cells [17, 21, 43]. Based on the above discussion and previous studies, we believe that FITC-ZnO nanocomposite trigger preferential apoptosis in cancer cells by generation of intracellular ROS and release of Zn^{2+} ions due to their higher surface reactivity and surface area.

5. Conclusion

We have successfully developed FITC encapsulated ZnO nanocomposite using a single step soft chemical method. XRD analysis and optical studies confirm the presence of FITC into the porous ZnO nanoassembly. FITC-ZnO nanocomposite shows a good stability in different culture media which is confirmed by the UV-visible spectra. Cytotoxicity study of FITC-ZnO nanocomposite shows its ability for preferentially killing cancer cells much more efficiently than the normal cells. Toxic effect of FITC-ZnO nanocomposite is attributed due the generation of reactive oxygen species and release of Zn^{2+} ions, which diminish the normal functioning of mitochondria leading to apoptosis. FACS analysis and confocal results show that apoptotic cells and DNA fragmentation are caused by ROS induced by FITC-ZnO nanocomposite. This nanocomposite induces cell cycle arrest in the S phase. Thus, FITC-ZnO nanocomposite may be used as fluorescence probe for imaging along with cancer therapeutics.

Acknowledgement

Jagriti Gupta acknowledges CSIR, India for the award of Senior Research Fellowship (SRF). I would like to thank Dr. Sudeshna Chandra, MEMS, IIT Bombay for reading the

manuscript and useful suggestions. The financial support by Nanomission of DST, and nanotechnology division of DEITY, Govt. of India are gratefully acknowledged.

References

- [1] V. Bhosle, A. Tiwari and J. Narayan, *J. of Appl. Phys.*, 2006, 100, 033713-033718.
- [2] B. A. Buchine, W. L. Hughes, F. L. Degertekin and Z. L. Wang, *Nano Lett*, 2006, 6, 1155-1159.
- [3] J. Liu, C. Guo, C. M. Li, Y. Li, Q. Chi, X. Huang, L. Liao and T. Yu, *Electrochem. Commun.*, 2009, 11, 202-205.
- [4] H. Hong, J. Shi, Y. Yang, Y. Zhang, J. W. Engle, R. J. Nickles, X. Wang and W. Cai, *Nano Letters*, 2011, 11, 3744-3750.
- [5] D. Peer, J. M. Karp, S. Hong, O. C. Farokhzad, R. Margalit and R. Langer, *Nat. Nanotechnol.*, 2007, 2, 751-760.
- [6] S. Nair, A. Sasidharan, V. V. Divya Rani, D. Menon, S. Nair, K. Manzoor and S. Raina, *J. Mater. Sci.- Mater. Med.*, 2009, 20 Suppl 1, S235-241.
- [7] S. Singh, K. C. Barick and D. Bahadur, *CrystEngComm*, 2013, 15, 4631-4639.
- [8] J. Gupta, K. C. Barick and D. Bahadur, *J. Alloys Compd.*, 2011, 509, 6725-6730.
- [9] S. Singh, K. C. Barick and D. Bahadur, *J. Mater. Chem. A*, 2013, 1, 3325-3333.
- [10] J. W. Rasmussen, E. Martinez, P. Louka and D. G. Wingett, *Expert opin. Drug Delivery*, 2010, 7, 1063-1077.
- [11] K. C. Barick, S. Nigam and D. Bahadur, *J. Mater. Chem.*, 2010, 20, 6446-6452.
- [12] G. Oberdorster, J. Ferin and B. E. Lehnert, *Environ. Health Perspect.*, 1994, 102 Suppl 5, 173-179.
- [13] T.-K. Hong, N. Tripathy, H.-J. Son, K.-T. Ha, H.-S. Jeong and Y.-B. Hahn, *J. Mater. Chem. B*, 2013, 1, 2985-2992.
- [14] D. A. Groneberg, M. Giersig, T. Welte and U. Pison, *Curr. Drug Targets*, 2006, 7, 643-648.
- [15] P. Moller, N. R. Jacobsen, J. K. Folkmann, P. H. Danielsen, L. Mikkelsen, J. G. Hemmingsen, L. K. Vesterdal, L. Forchhammer, H. Wallin and S. Loft, *Free Radical Res.*, 2010, 44, 1-46.

- [16] N. Li, C. Sioutas, A. Cho, D. Schmitz, C. Misra, J. Sempf, M. Wang, T. Oberley, J. Froines and A. Nel, *Environ. Health Perspect.*, 2003, 111, 455-460.
- [17] A. Sasidharan, P. Chandran, D. Menon, S. Raman, S. Nair and M. Koyakutty, *Nanoscale*, 2011, 3, 3657-3669.
- [18] V. Sharma, D. Anderson and A. Dhawan, *Apoptosis*, 2012, 17, 852-870.
- [19] V. Aruoja, H. C. Dubourguier, K. Kasemets and A. Kahru, *Sci. Total Environ.*, 2009, 407, 1461-1468.
- [20] M. Li, L. Zhu and D. Lin, *Environ. Sci. Technol.*, 2011, 45, 1977-1983.
- [21] T. Xia, M. Kovoichich, M. Liong, L. Mädler, B. Gilbert, H. Shi, J. I. Yeh, J. I. Zink and A. E. Nel, *ACS Nano*, 2008, 2, 2121-2134.
- [22] K. H. Muller, J. Kulkarni, M. Motskin, A. Goode, P. Winship, J. N. Skepper, M. P. Ryan and A. E. Porter, *ACS Nano*, 2010, 4, 6767-6779.
- [23] T. D. Zaveri, N. V. Dolgova, B. H. Chu, J. Lee, J. Wong, T. P. Lele, F. Ren and B. G. Keselowsky, *Biomaterials*, 2010, 31, 2999-3007.
- [24] B. Desnues, C. Cuny, G. Gregori, S. Dukan, H. Aguilaniu and T. Nystrom, *EMBO reports*, 2003, 4, 400-404.
- [25] A. Aertsen and C. W. Michiels, *Crit. Rev. Microbiol.*, 2004, 30, 263-273.
- [26] J.-h. Li, X.-r. Liu, Y. Zhang, F.-f. Tian, G.-y. Zhao, Q.-l.-y. Yu, F.-l. Jiang and Y. Liu, *Toxicol. Res.*, 2012, 1, 137-144.
- [27] D. W. Choi and J. Y. Koh, *Annu. Rev. of Neurosci.*, 1998, 21, 347-375.
- [28] M. Premanathan, K. Karthikeyan, K. Jeyasubramanian and G. Manivannan, *Nanomedicine*, 2011, 7, 184-192.
- [29] S. Ostrovsky, G. Kazimirsky, A. Gedanken and C. Brodie, *Nano Res.*, 2009, 2, 882-890.
- [30] M. J. Akhtar, M. Ahamed, S. Kumar, M. M. Khan, J. Ahmad and S. A. Alrokayan, *Int. J. Nanomedicine*, 2012, 7, 845-857.

- [31] D. Guo, H. Bi, B. Liu, Q. Wu, D. Wang and Y. Cui, *Toxicol. in vitro*, 2013, 27, 731-738.
- [32] A. Punnoose, K. Dodge, J. W. Rasmussen, J. Chess, D. Wingett and C. Anders, *ACS Sustainable Chem. Eng.*, 2014, 2, 1666-1673.
- [33] A. Burns, H. Ow and U. Wiesner, *Chem. Soc. Rev.*, 2006, 35, 1028-1042.
- [34] H. Guo, H. Qian, S. Sun, D. Sun, H. Yin, X. Cai, Z. Liu, J. Wu, T. Jiang and X. Liu, *Chem. Cent. J.*, 2011, 5, 1.
- [35] N. Shanta Singh, H. Kulkarni, L. Pradhan and D. Bahadur, *Nanotechnology*, 2013, 24, 065101.
- [36] K. N. Yu, T. J. Yoon, A. Minai-Tehrani, J. E. Kim, S. J. Park, M. S. Jeong, S. W. Ha, J. K. Lee, J. S. Kim and M. H. Cho, *Toxicol. in vitro*, 2013, 27, 1187-1195.
- [37] J. Zhang, A. Thurber, D. A. Tenne, J. W. Rasmussen, D. Wingett, C. Hanna and A. Punnoose, *Adv. Funct. Mater.*, 2010, 20, 4358-4363.
- [38] J. Enderlein, *Appl. Phys. Lett.*, 2002, 80, 315-317.
- [39] N. R. Jacobsen, G. Pojana, P. White, P. Moller, C. A. Cohn, K. S. Korsholm, U. Vogel, A. Marcomini, S. Loft and H. Wallin, *Environ. Mol. Mutagen.*, 2008, 49, 476-487.
- [40] P. V. AshaRani, G. Low Kah Mun, M. P. Hande and S. Valiyaveetil, *ACS Nano*, 2008, 3, 279-290.
- [41] H. J. Eom and J. Choi, *Environ. Sci. Technol.*, 2010, 44, 8337-8342.
- [42] H. Song, W. Wang, P. Zhao, Z. Qi and S. Zhao, *Nanoscale*, 2014, 6, 3206-3216.
- [43] X. Deng, Q. Luan, W. Chen, Y. Wang, M. Wu, H. Zhang and Z. Jiao, *Nanotechnology*, 2009, 20, 115101.

Figure Caption

Fig.1. (a) XRD patterns and (b) the three most intense peaks of ZnO and FITC-ZnO nanocomposite.

Fig.2. (a, b) SEM micrographs and (c and d) TEM micrographs of ZnO and FITC-ZnO nanocomposite.

Fig.3. (a) UV-visible spectra and (b) Fluorescence spectra of FITC, ZnO and FITC-ZnO nanocomposite.

Fig.4. pH dependent fluorescent intensity change of pure FITC and FITC-ZnO nanocomposite. Means \pm standard error from representative experiments are presented ($n = 3$). P values were determined by Student's t-test. indicates $p < 0.05$.

Fig.5. Cellular uptake study by CLSM (a) bright field image and (b) fluorescence image treated with 100 $\mu\text{g/ml}$ of FITC-ZnO nanocomposites for 3h. Fig.4 Quantification of cellular uptake of FITC-ZnO nanocomposites by measuring the Zn content per/cell using ICP-AES analysis (c) for HeLa and MCF-7 and (d) for L929. Means \pm standard error from representative experiments are presented ($n = 3$). P values were determined by Student's t-test. indicates $p < 0.05$.

Fig.6. ROS production induced by FITC-ZnO nanocomposite on (a) HeLa, (b) MCF-7 and (c) L929 cells after 48 h exposure. Means \pm standard error from representative experiments are presented ($n = 3$). P values were determined by Student's t-test, indicates $p < 0.05$ and $p^{**} < 0.001$

Fig.7. (a-h) show CLSM images for detection of ROS in HeLa cells. (b) HeLa cells with H₂-DCFDA, (c) H₂-DCFDA-H₂O₂ and (d) H₂DCFDA-NAC. Fig. 6. (e) HeLa cells treated ZnO with H₂DCFDA, (f) FITC-ZnO nanocomposite, (g) FITC-ZnO nanocomposite with H₂DCFDA, and (h) FITC-ZnO nanocomposite with H₂DCFDA with NAC for 24 h. Scale bar: 50 μm .

Fig.8. Time and dose dependent cytotoxicity of FITC-ZnO nanocomposites in (a) HeLa, (b) MCF-7, and (c) Cytotoxicity of L929 cells after 24 h exposure. Means \pm standard error from

representative experiments are presented ($n = 3$). P values were determined by Student's t-test, indicates $p < 0.05$ and $p < 0.001$

Fig.9. FACS analysis representing apoptosis based on Annexin V-FITC and PI staining assay of HeLa cells (a) Control (b) treated with FITC-ZnO nanocomposite at concentration of 100 $\mu\text{g/ml}$ for 24 h.

Fig.10. Confocal laser scanning microscopy (CLSM) images show the apoptosis (DNA fragmentation) in HeLa cells. (a) Control showing rounded, intact nucleus, (b-d) with FITC-ZnO nanocomposite (100 $\mu\text{g/ml}$) at indicated time intervals of 3, 24, and 48 h. The green fluorescence shows presence of FITC in FITC-ZnO nanocomposite, red fluorescence shows ethidium bromide (EtBr) stained nuclei. The scale bar is 50 μm . Fig. 8 (b to d) inset images show typical apoptotic nuclei with fragmented morphology.

Fig. 11. (a) Mitochondrial membrane potential of HeLa cell treated with ZnO nanoassembly and (b) LDH release in HeLa cells after 24h treatment with FITC-ZnO nanocomposite.

Fig.12. FITC-ZnO nanocomposite induces HeLa cell cycle arrest in S phase. The cell cycle changes of HeLa cells were evaluated after treatment with FITC-ZnO nanocomposite for 24 and 48 h were performed by using flow cytometer. (a and d) shows control HeLa cells without any treatment for 24 and 48 h, (b, c, e and f) show the decrease in the percentage of cells in G1 phase and increase in the percentage of cells in S phase with the increase in the concentration 50 $\mu\text{g/ml}$ to 100 $\mu\text{g/ml}$ after 24 and 48 h treatment, yet the percentage of cells in G2 phase has no significant change.

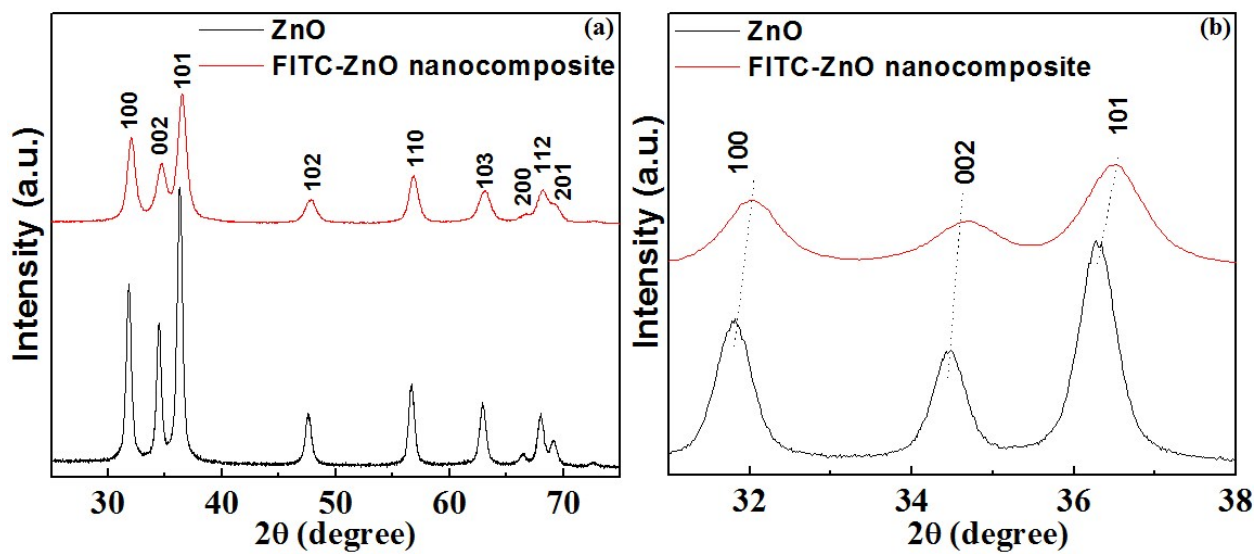


Fig.1

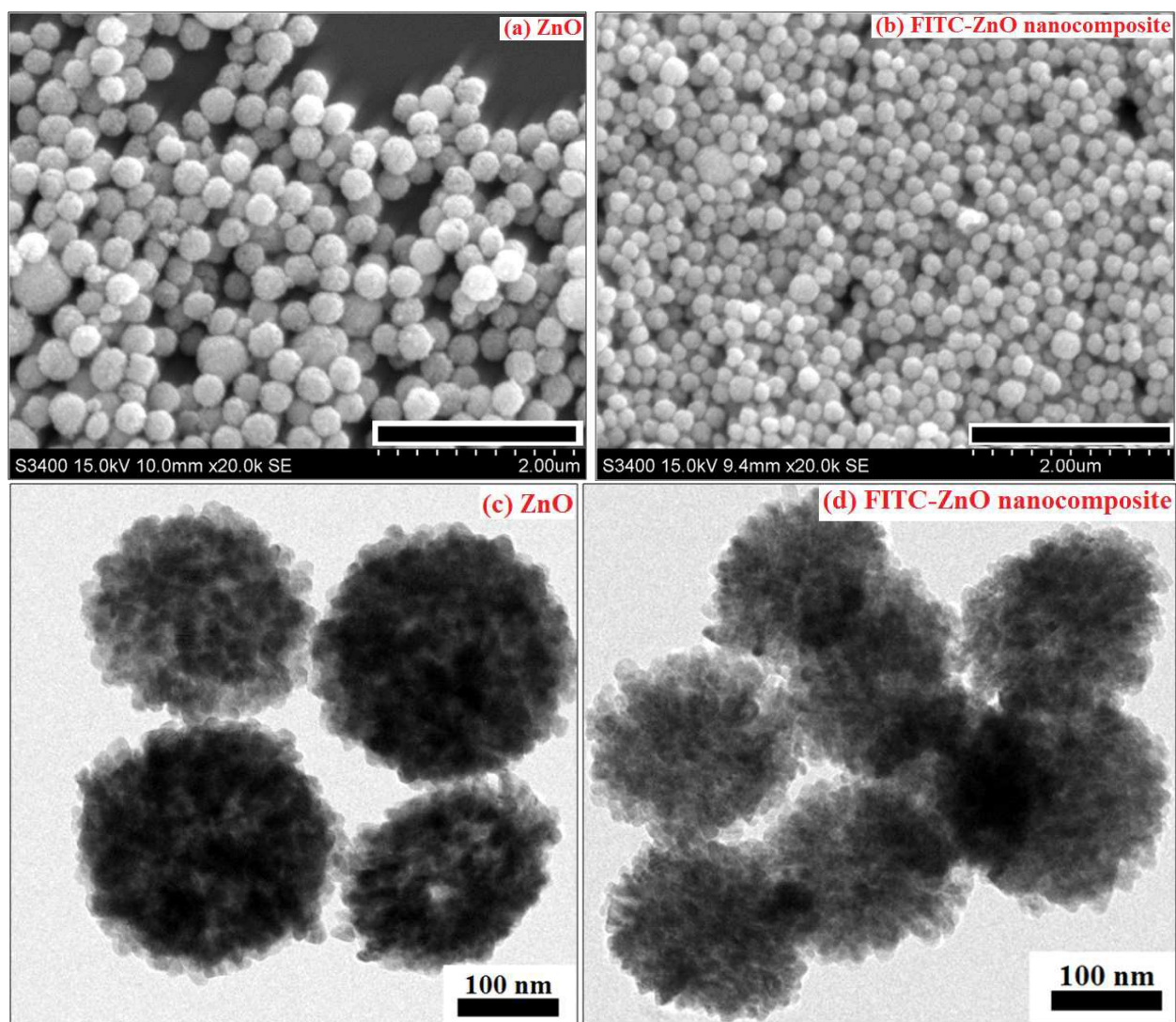


Fig.2

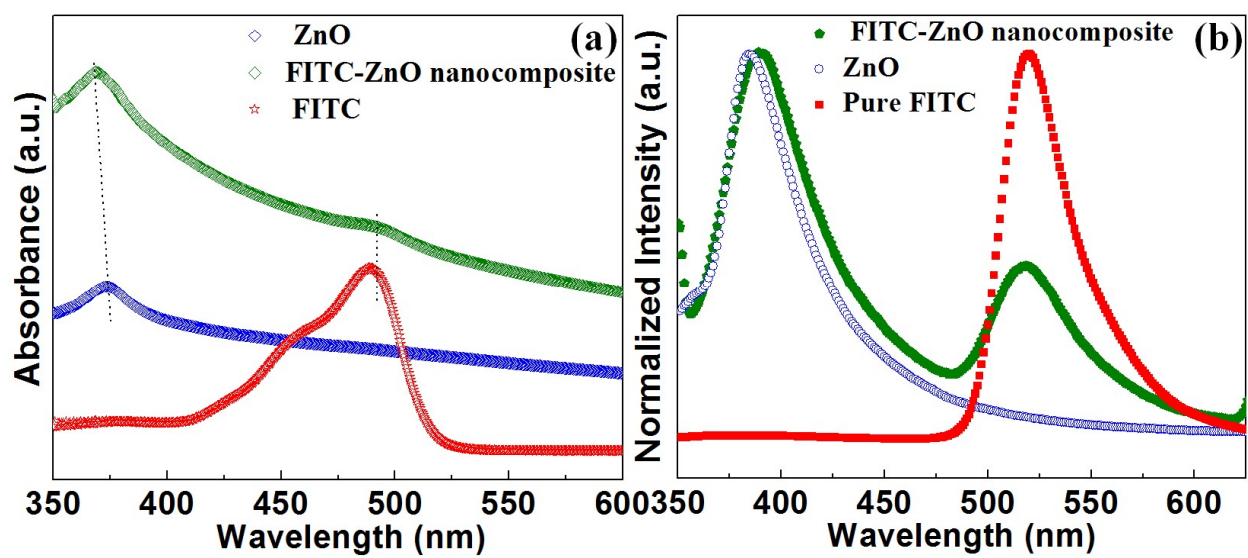


Fig.3

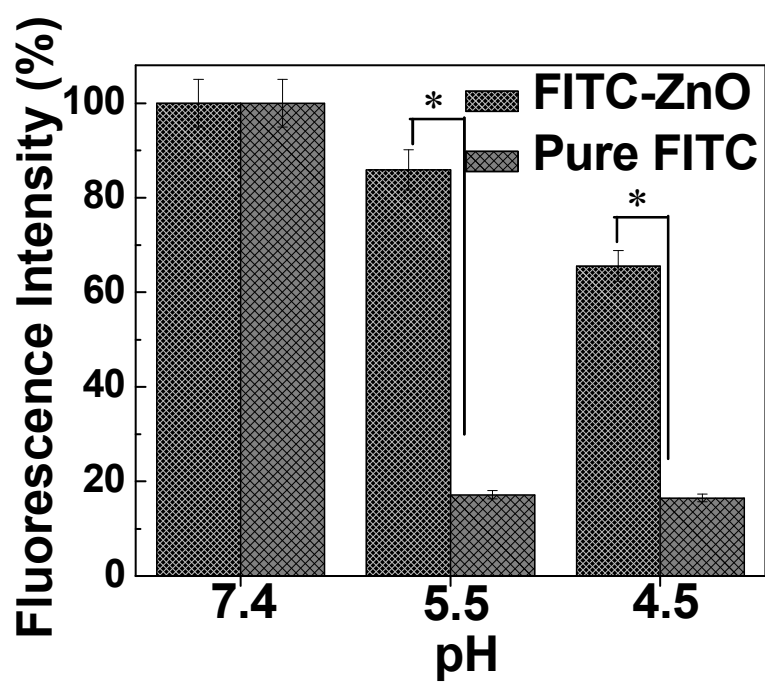


Fig.4

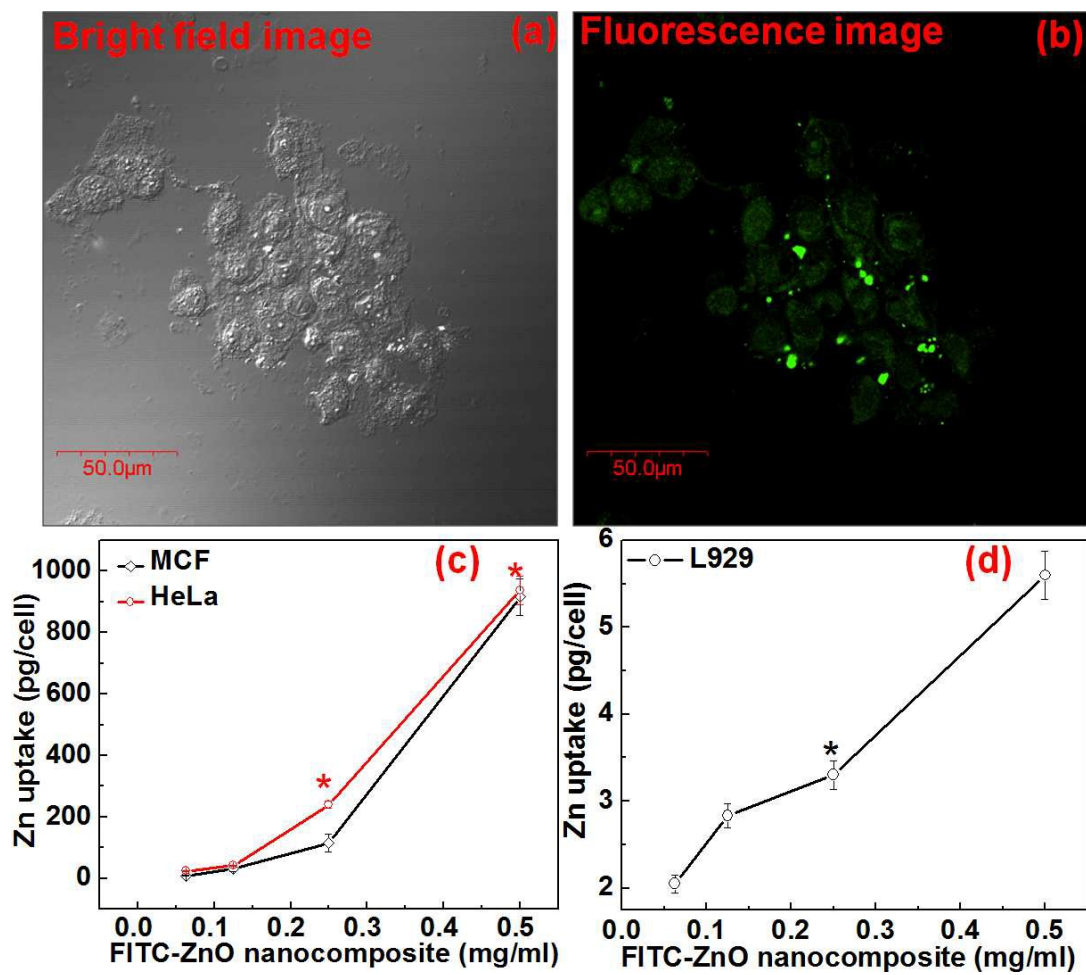


Fig.5

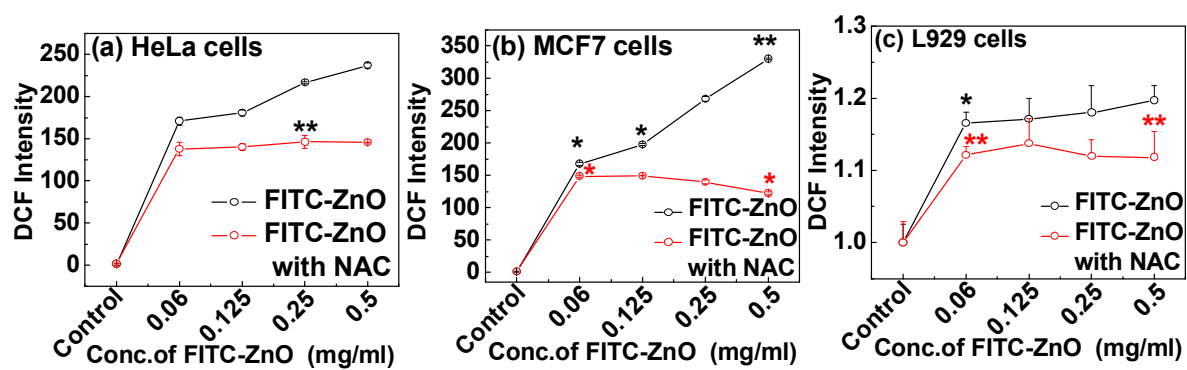


Fig.6

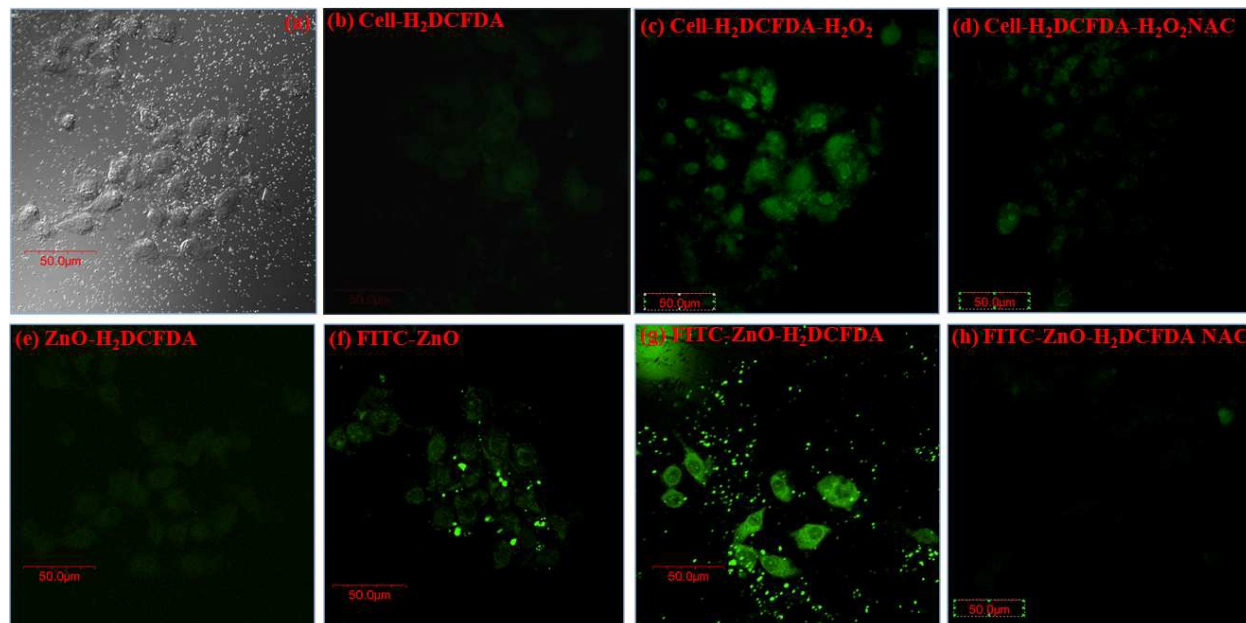


Fig.7

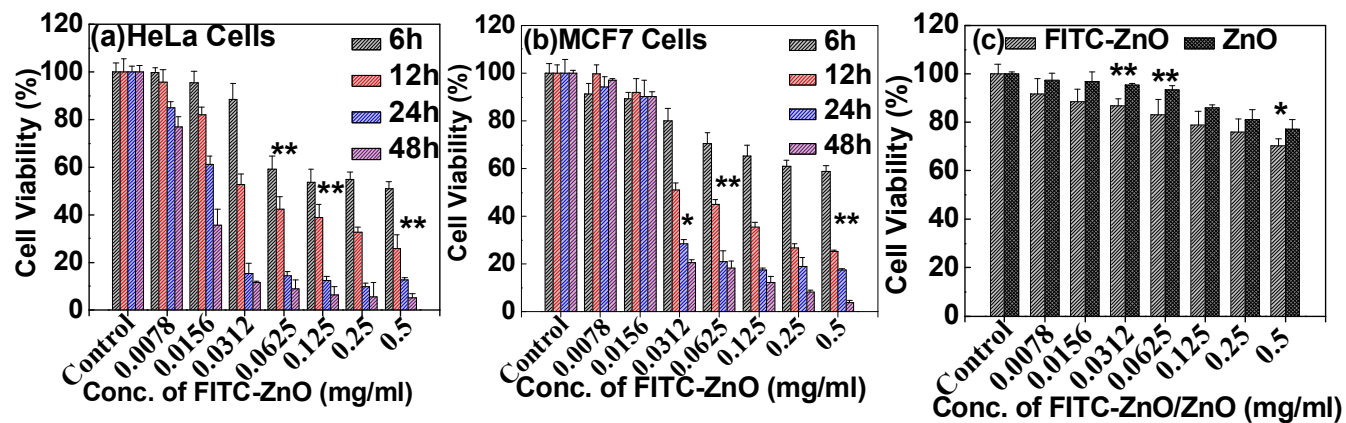


Fig.8

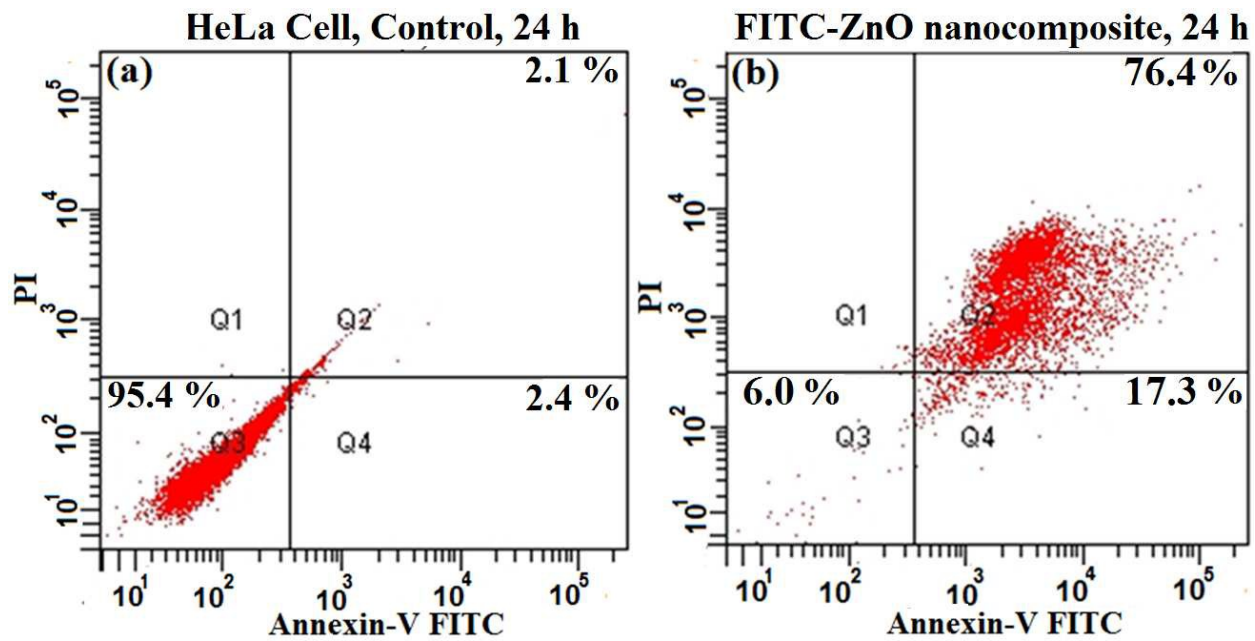


Fig.9

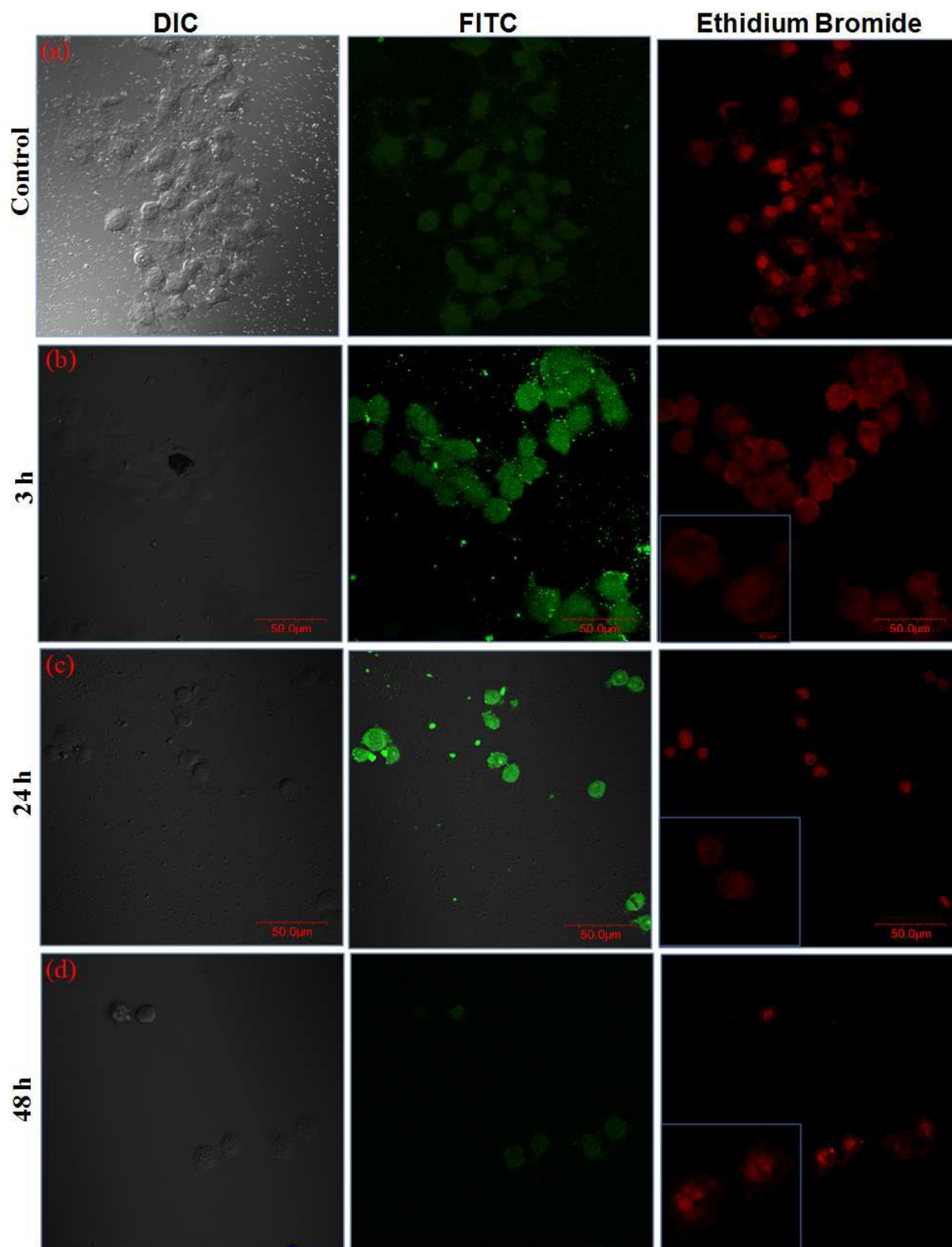


Fig.10

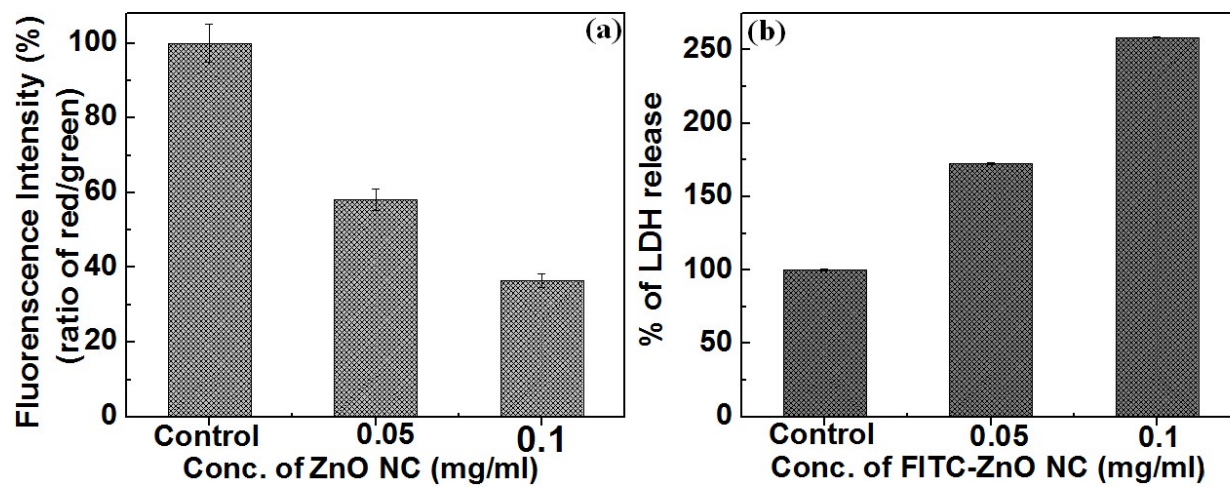


Fig.11

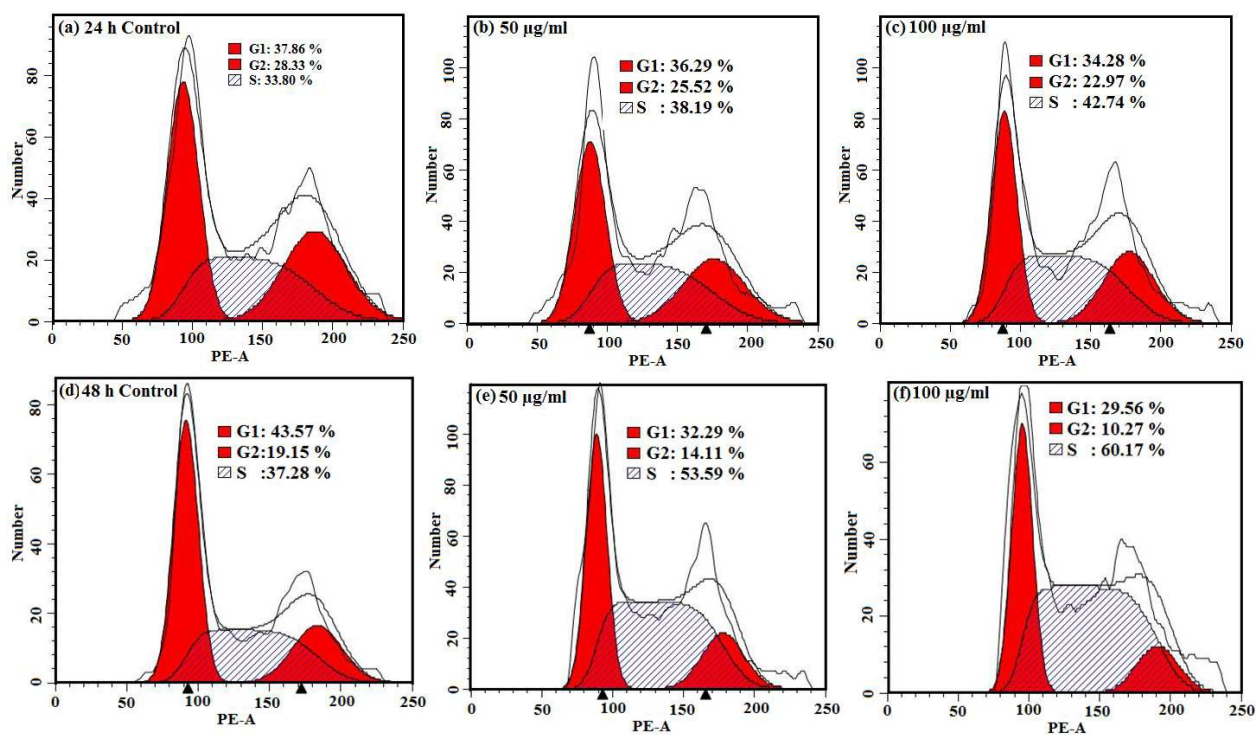


Fig.12

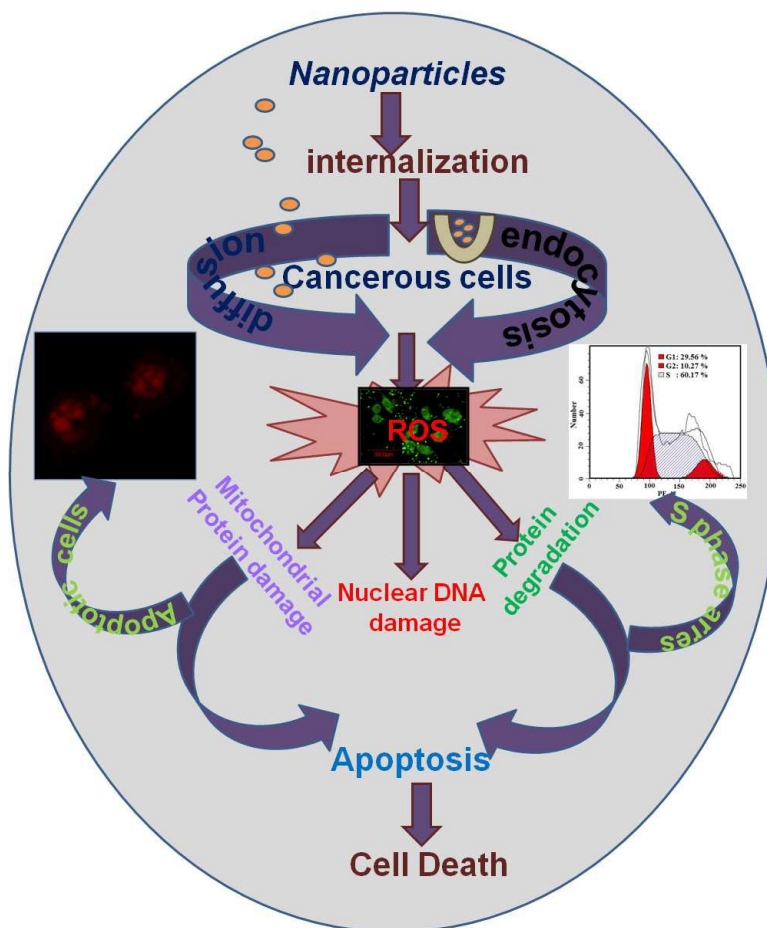
Fluorescent ZnO for imaging and induction of DNA fragmentation and ROS-mediated apoptosis in Cancer cells

Jagriti Gupta, Parag Bhargava and D. Bahadur*

Department of Metallurgical Engineering and Materials Science,
Indian Institute of Technology Bombay, Mumbai – 400076, India

*Corresponding address: Tel. + 91-22-2576 7632, Fax: + 91-22 2572 3480, Email: dhiren@iitb.ac.in

Graphical Abstract:



Systemic diagram shows the cell death mechanism through the generation of reactive oxygen species.